DECEMBER 1993

ANALYSIS OF GLOBAL ALFVÉN MODES BY THE EXTENSION OF CASTOR WITH AN EXTERNAL ANTENNA

G.T.A. HUYSMANS, H.A. HOLTIES, AND J.P. GOEDBLOED

RIJNHUIZEN REPORT 93-219

REPORT ON JET CONTRACT
NO. JT2/12405

PROJECT LEADER: J.P. GOEDBLOED

CONTENTS

PREFACE

Energetic ions, such as fusion born α-particles, can destabilise global Alfvén modes in tokamaks (e.g. TAE modes) close to break-even conditions. In order to asses this possibility, the Alfvén spectrum of the JET configuration has been studied by means of the spectral code CASTOR (Complex Alfvén Spectrum in TORoidal geometry). An important extension of this code is the addition of an external antenna system, which allows 1) to study the damping of the TAE modes more effectively and 2) to perform MHD spectroscopy of Alfvén modes excited by an external antenna system.

This requires the replacement of the vacuum module of the CASTOR code by a module which incorporates the appropriate boundary conditions for an external antenna system. Because of the way the calculation of external resistive modes is incorporated in the present version of CASTOR, this extension is possible without upsetting the convergence of the numerical scheme.

The modified code has been applied to the analysis of the computed MHD spectrum of global Alfvén modes excited by the saddle coil antenna, taking the measured equilibrium profiles of the JET high performance discharges.

This report describes the work that has been performed under contract JT2/12405.

1. INTRODUCTION

Global Alfvén modes can be excited by energetic particles, in particular, by fusion born α particles. The destabilized modes can lead to an enhanced loss of confinement of the α particles, with the consequence that they are lost before having contributed to the heating of the plasma. Experimentally, the global Alfvén modes have been destabilized by the fast particles population created by neutral beam injection [1,2]. The damping of the modes was found to be an order of magnitude larger than the estimates based on electron Landau damping. Subsequently, new damping mechanisms have been proposed, i.e., continuum damping, ion Landau damping and electron kinetic (radiative) damping.
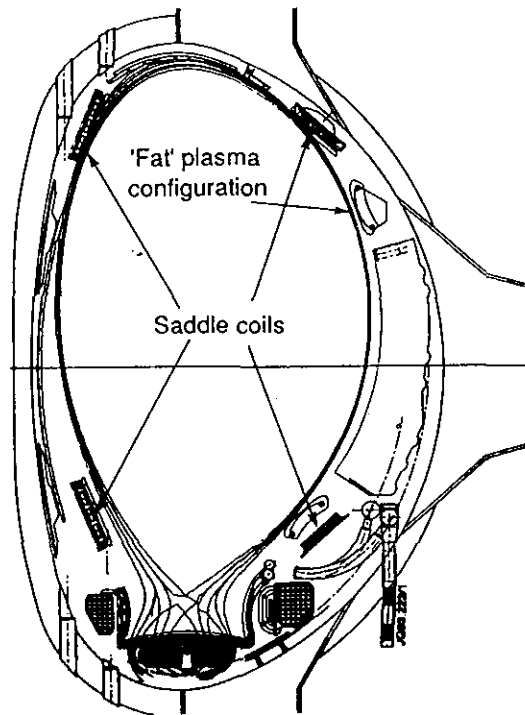
Fig. 1 *A cross section of the JET divertor geometry showing the poloidal position of the saddle coils. In the toroidal direction, there are four saddle coils both at the top and bottom of the vessel.*

In JET, an experiment is planned to excite global Alfvén waves (TAE as well as EAE modes) by means of an external antenna. In contrast to previous experiments, the waves are not driven unstable but are oscillating with the frequency of the antenna. The saddle coils (see Fig. 1), which are newly installed in the JET vessel for disruption control, will be used as the driving antenna. By scanning the driving frequency in the Alfvén frequency range of 30-500 kHz, the TAE and EAE modes will show up as resonances of the power absorbed by the plasma, as can be measured by the antenna impedance. The

width of the resonance is directly proportional to the damping of the mode. In this way a direct measurement of the damping is obtained without the need to drive the global modes unstable, i.e. independent of the fast particle drive. Also, measuring the damping as a function of the fast particle population gives the possibility to study the fast particle drive.

To model the excitation of global Alfvén waves by an external antenna, the toroidal resistive MHD code CASTOR has been extended to include an antenna in the vacuum surrounding the plasma. The first part of this report contains a description of the plasma-vacuum-antenna model and the implementation in the CASTOR code. In the second part of this report, the code is applied to the JET saddle coil geometry.

2. MODELLING THE EXCITATION BY AN EXTERNAL ANTENNA

To model the excitation of Alfvén waves, the plasma is described by the compressible resistive MHD equations in toroidal geometry. Since the amplitude of the excited waves will be small $(\delta B/B \sim 10^{-5})$ the linearized equations yield an appropriate description of the plasma oscillations.

The geometry of the plasma-vacuum-antenna system is shown in Fig. 2. The plasma is surrounded by a vacuum and an ideally conducting wall. The antenna lies on a contour around the plasma in the vacuum. The radial width of the antenna is considered to be infinitely thin. The shapes of the plasma boundary, of the ideally conducting wall, and of the antenna contour in the poloidal plane are arbitrary as long as the three shapes are nested surfaces.

In this chapter, the extension of the CASTOR code to include an antenna is described. First, a short description of the existing CASTOR code is given. The modelling of the antenna requires a free boundary description since the plasma is driven by the magnetic field perturbation at the plasma boundary induced by the antenna. The implementation of the plasma-vacuum boundary conditions is such that the vacuum equations can be solved independently from the plasma equations. In the following sections, the implementation of the plasma vacuum boundary conditions and the resulting requirements from the vacuum solution are discussed. Finally in this chapter the actual solution of the vacuum equations and the relevant test cases are described.
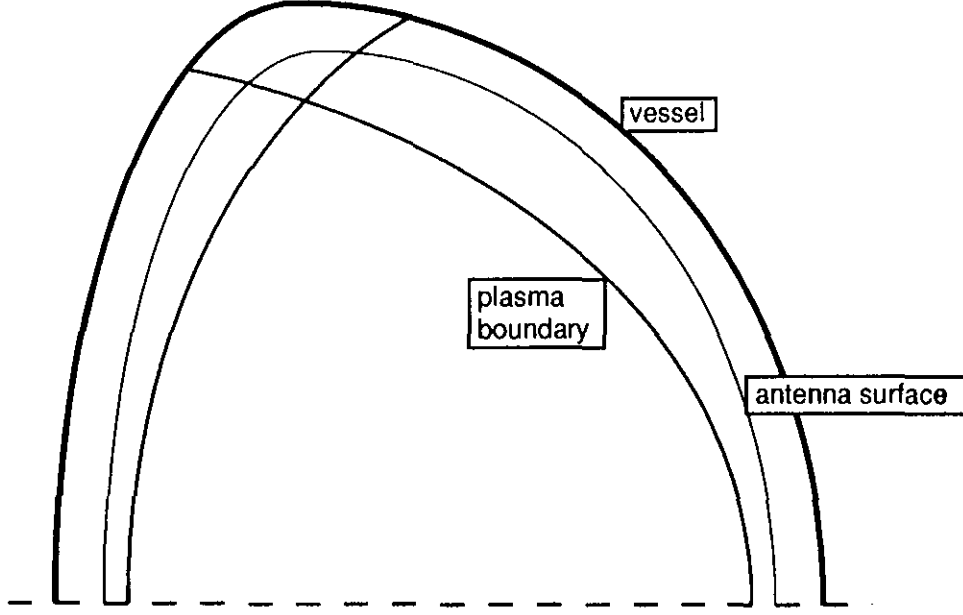
Fig. 2 *The geometry of the plasma-antenna-vacuum system*

2.1 The CASTOR code

The linearized resistive MHD equations as implemented in the CASTOR code [3] are given by:

$$\lambda \rho_1 = -\nabla \cdot (\rho_0 v_1)$$

$$\lambda \rho_0 v_1 = -\nabla (\rho_0 T_1 + \rho_1 T_0) + (\nabla \times B_0) \times (\nabla \times A_1) - B_0 \times (\nabla \times \nabla \times A_1)$$

$$\lambda \rho_0 T_1 = -\rho_0 v_1 \cdot \nabla T_0 - (\gamma - 1)\rho_0 T_0 \nabla \cdot v_1 + 2\eta(\gamma - 1)(\nabla \times B_0) \cdot (\nabla \times \nabla \times A_1) \qquad (1)$$

$$\lambda A_1 = -B_0 \times v_1 - \eta \nabla \times \nabla \times A_1$$

where v_1, A_1, ρ_1 and T_1 are the perturbed velocity, vector potential, density and temperature, and B_0, ρ_0 and T_0 are the equilibrium magnetic field, density and temperature, respectively. The ratio of the specific heats is given by γ. The time dependence of the variables is given by $u(r, t) = u(r)e^{\lambda t}$.

In the CASTOR code, the variables are discretized using cubic and quadratic finite elements in the radial direction and Fourier harmonics in the poloidal and toroidal angle. Due to the axisymmetry of the equilibrium the dependence on the toroidal angle can be

described by one mode number n:

$$u(s, \theta, \phi) = \sum_{i,m} u_{i,m} h(s - s_i) e^{im\theta} e^{in\phi} , \tag{2}$$

where $s = \sqrt{\psi}$ is used as the radial coordinate. The poloidal angle θ is chosen such that the magnetic field lines appear straight in the (θ, ϕ) plane. The toroidal angle ϕ is the usual polar angle. The functions $h(s - s_i)$ represent the finite elements with s_i the nodal points.

In the CASTOR code, the linear equations (1) are solved in the weak form. The weak form is obtained by multiplying each equation with a test function and integrating the equation over the plasma volume. The test functions are chosen to be the same finite elements as those used to represent the radial dependence of the eight variables (Galerkin method).

In the previous version of CASTOR, i.e. the one without the external antenna, the construction of the weak form yields a generalized matrix eigenvalue problem

$$\boldsymbol{A}\boldsymbol{u} = \lambda \boldsymbol{B}\boldsymbol{u} , \tag{3}$$

where λ is the eigenvalue of the system. The vector $\boldsymbol{u}$ is the state vector containing the expansion coefficients of the eight variables. The matrices $\boldsymbol{A}$ and $\boldsymbol{B}$ are complex. The CASTOR code contains several solvers for the solution of this large complex (non-Hermitian) eigenvalue problem. The QR algorithm yields the complete spectrum of eigenvalues. The use of this algorithm is restricted to relative small problems due to the memory requirements. To obtain single eigenvalues, the inverse vector iteration algorithm is used. With this method very large matrices can be handled.

Including the driving term in the system due to the external antenna changes the eigenvalue problem into a driven response problem. The time dependence of the plasma is now taken to be the frequency of the driver, $\lambda = i\omega_d$. This yields the following system of equations:

$$(\boldsymbol{A} - i\omega_d \boldsymbol{B})\boldsymbol{u} = \boldsymbol{f}_d . \tag{4}$$

The solution $\boldsymbol{u}$ is now the stationary state solution in which all quantities oscillate with the driver frequency. The driving term $\boldsymbol{f}_d$ on the right hand side is obtained from the solution of the vacuum equation including an antenna. This is discussed in the next paragraph.

7

2.2 Boundary conditions at the plasma-vacuum interface

The two regions of the system, the plasma and the vacuum, are connected by the boundary conditions at the interface. For a resistive plasma with zero equilibrium pressure and vanishing current density at the plasma boundary the linearized boundary conditions are :

$$b{\cdot}n = \hat{b}{\cdot}n, \qquad b \times n = \hat{b} \times n, \qquad (5)$$

where b is the plasma magnetic field perturbation, $\hat{b}$ is the pertubed magnetic field in the vacuum, and n is the normal to the plasma boundary. The pressure balance condition $p_1 = 0$ is automatically satisfied for the equilibria considered, i.e. zero current density at the plasma boundary.

In the weak form formulation of the eight resistive MHD equations, two surface integrals appear as a result of a partial integration of the momentum and the induction equation:

$$
\begin{aligned}
W_s^I &= - \iint_S (v^*{\cdot}n_0)(B_0{\cdot}b)dS, \\
W_s^R &= \iint_S \eta(A^* \times b){\cdot}n_0 dS.
\end{aligned}
\qquad (6)
$$

Here, v^* and A^* are the adjoint test functions. By rewriting the two surface terms using the plasma-vacuum boundary conditions and information of the vacuum solution these boundary conditions can be implemented as natural conditions.

For example, W_s^I can be rewritten as (using continuity of the equilibrium magnetic field B_0)

$$W_s^I = - \iint_S (v^*{\cdot}n_0)(B_0{\cdot}\hat{b})dS. \qquad (7)$$

Defining the vacuum response as

$$B_0{\cdot}\hat{b} = \alpha(\hat{b}{\cdot}n_0) = \alpha(b{\cdot}n_0), \qquad (8)$$

the surface integral can again be written in terms of plasma variables:

$$W_s^I = - \iint_S \alpha(v^*{\cdot}n_0)(b{\cdot}n_0)dS. \qquad (9)$$

8

The influence of the vacuum region between the plasma and an ideally conducting wall can thus be described by a relation between the normal and tangential components of the perturbed vacuum magnetic field at the plasma boundary [4]. If there is no antenna present in the vacuum, this relation can be expressed as:

$$(\hat{b} \times n)_m = \sum_{\bar{m}} \alpha_{m\bar{m}} (\hat{b} \cdot n)_{\bar{m}}. \tag{10}$$

The vacuum response matrix $\alpha_{m\bar{m}}$ is obtained from the vacuum solutions with the boundary condition $(\hat{b} \cdot n)_{\bar{m}} = \delta_{\bar{m}m}$ at the plasma boundary and $\hat{b} \cdot n = 0$ at the ideally conducting wall. The row m of the matrix α contains the Fourier series of $\hat{b} \times n$ due to the unit perturbation in the mth harmonic of $\hat{b} \cdot n$.
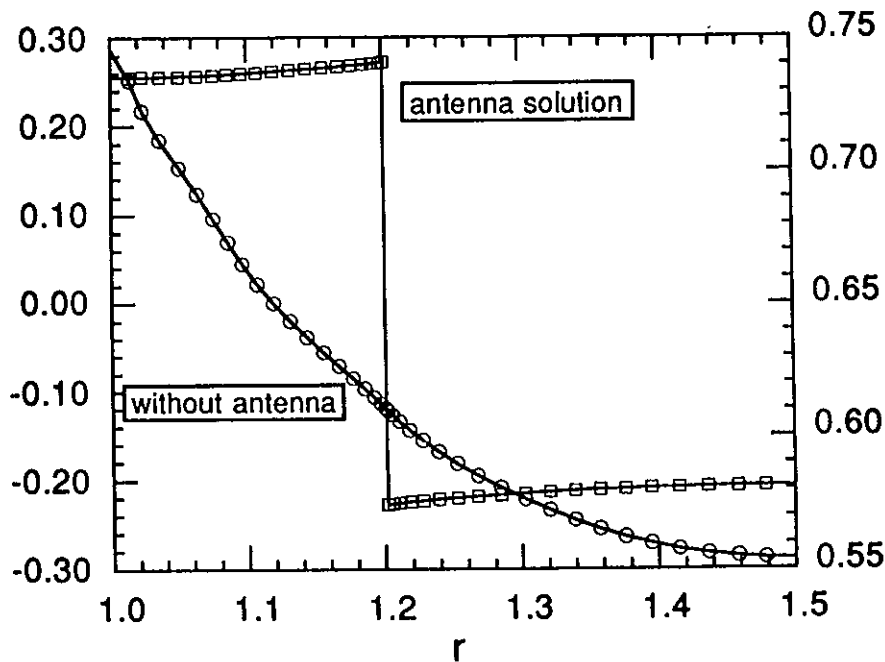
Fig. 3 *A sketch of the two independent solutions of the vacuum equations with and without the antenna.*

The current in the antenna yields an additional contribution to the tangential magnetic field at the plasma boundary which is independent of the normal magnetic field perturbation of the plasma. This yields an additional term, β_m^{ant} in relation (6):

$$(\hat{b} \times n)_m = \sum_{\bar{m}} \alpha_{m,\bar{m}} (\hat{b} \cdot n)_{\bar{m}} + \beta_m^{ant}. \tag{11}$$

The β_m^{ant} term results from the vacuum solution with the boundary conditions $\hat{b} \cdot n = 0$ at both the plasma and the ideally conducting wall. The surface current in the antenna causes

a jump in the tangential magnetic field at the antenna. The vacuum response matrix α is independent of the presence of the antenna.

By this construction, where the antenna solution has $\hat{b}\cdot n = 0$ at the plasma boundary, the complete vacuum solution consists of two independent solutions which can be seen as the homogeneous and the inhomogenuous solutions of the vacuum equations. Fig. 3 shows a sketch of the two types of solutions. The next section discusses the numerical solution of the vacuum equations.

2.3 The vacuum solution

The magnetic field in the vacuum is described by the equations

$$
\begin{aligned}
\boldsymbol{\nabla}\cdot\hat{\boldsymbol{b}} &= 0, \\
\boldsymbol{\nabla}\times\hat{\boldsymbol{b}} &= 0.
\end{aligned}
\tag{12}
$$

Introducing the scalar potential $\hat{\boldsymbol{b}} = \boldsymbol{\nabla}\Phi$ yields a single Laplace equation

$$
\boldsymbol{\nabla}\cdot\boldsymbol{\nabla}\Phi = 0.
\tag{13}
$$

As discussed in the previous section Eq. (13) has to be solved with respect to two sets of boundary conditions, viz.

- for the response matrix α:

$$
\begin{aligned}
&\text{on the plasma boundary}: \quad (\boldsymbol{b}\cdot\boldsymbol{n})_m = \delta_{\bar{m}m}, \\
&\text{on the ideally conducting wall}: \quad \boldsymbol{b}\cdot\boldsymbol{n} = 0, \\
&\text{at the antenna surface}: \quad \text{no condition},
\end{aligned}
\tag{14}
$$

- for the antenna induced response β:

$$
\begin{aligned}
&\text{on the plasma boundary}: \quad (\boldsymbol{b}\cdot\boldsymbol{n})_m = 0, \\
&\text{on the ideally conducting wall}: \quad \boldsymbol{b}\cdot\boldsymbol{n} = 0, \\
&\text{at the antenna surface}: \quad [\![\boldsymbol{b}\times\boldsymbol{n}]\!] = \boldsymbol{j}_{ant}.
\end{aligned}
\tag{15}
$$

For an easy implementation of the numerical solution, the coordinate system to be used in the vacuum should have the three surfaces of the plasma boundary (r_p), the antenna (r_a), and the wall (r_w) as a coordinate surface. Also, the poloidal angle has to match the poloidal angle used in the plasma at the plasma boundary. The radial coordinate s can

10

be constructed using a quadratic interpolation of the three fixed radial points $r_p(\theta)$, $r_a(\theta)$, and $r_w(\theta)$:

$$s = s_a \left(\frac{r - r_p}{r_a - r_p}\right)\left(\frac{r - r_w}{r_a - r_w}\right) + \left(\frac{r - r_p}{r_w - r_p}\right)\left(\frac{r - r_a}{r_w - r_a}\right), \quad \chi = \chi_p(\theta), \tag{16}$$

where (r, θ) is the polar coordinate system centered on the geometric centre of the plasma, χ_p is the poloidal angle at the plasma boundary, s_a is the position of the antenna surface in the (s, χ) coordinate system, $s = 0$ on the plasma boundary and $s = 1$ on the wall.

Using the covariant representation for $\hat{b}$ and the contravariant representation for the antenna current j_{ant}, the jump in the magnetic field can be written as:

$$\begin{aligned}
[\![b_2]\!]_m &= [\![im\Phi_m]\!] = -(J|\nabla s|j_{\mathrm{ant}}^3)_m , \\
[\![b_3]\!]_m &= [\![in\Phi_m]\!] = (J|\nabla s|j_{\mathrm{ant}}^2)_m ,
\end{aligned} \tag{17}$$

where J is the jacobian of the (s, χ, ϕ) coordinate system. This yields a condition on the antenna current, identical with the constraint that the divergence of the antenna current is zero:

$$mj_m^2 + nj_m^3 = 0. \tag{18}$$

The antenna current is modelled as a surface current on the antenna surface. It can be represented by

$$j_m^3(s) = -\frac{m}{n}j_m^2 = I_m \frac{\delta(s - s_a)}{J|\nabla s|} \tag{19}$$

where the coefficients I_m can be chosen arbitrarily to represent the current distribution in the antenna.

For the numerical solution, the following weak form is constructed:

$$W_V = \iiint \Phi^* \nabla^2 \Phi dV = -\iiint \nabla\Phi^* \cdot \nabla\Phi dV + \iint \Phi^*(b \cdot n) dS . \tag{20}$$

The boundary term in this weak form containing $b \cdot n$ is ideally suited to implement the boundary conditions at the plasma and the wall. At the wall the boundary term vanishes. This natural boundary condition is automatically satisfied. For the boundary conditions (14) at the plasma, the boundary term with $(b \cdot n)_m = \delta_{m\bar{m}}$ creates the right hand side of the system of equations resulting from the weak form.

For the conditions (15), the boundary terms vanish and the conditions at the wall and at the plasma boundary are again naturally satisfied. The jump in the magnetic potential

at the antenna is an essential condition. This condition is implemented by introducing a special finite-element on the antenna surface. This cubic finite-element has a jump at $s = s_a$. The cubic finite-elements used in the weak form are drawn in Fig. 4. Due to the non-orthogonal coordinate system, a jump occurs in both Φ and in $\partial\Phi/\partial s$.
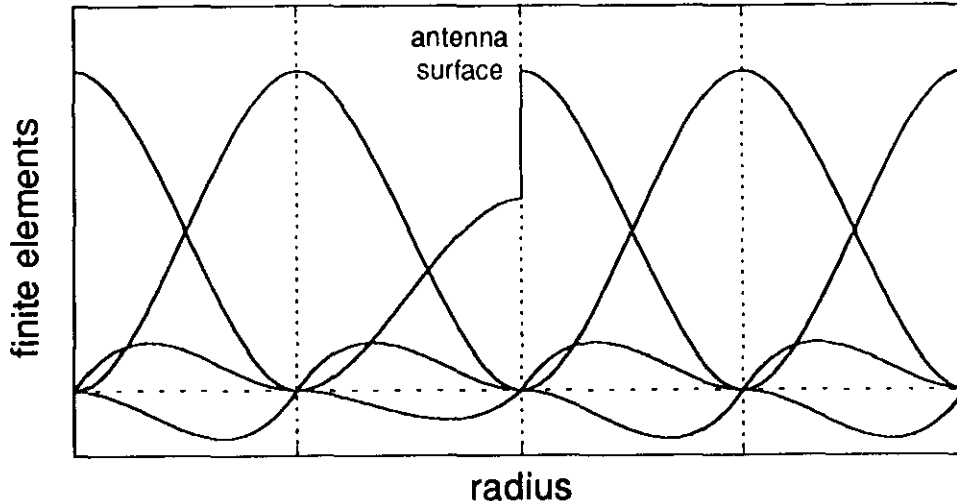
Fig. 4 *A sketch of the cubic Hermite finite elements used for solution of the vacuum equations. Note the jump in the element centered on the antenna surface*

The weak form formulation (Eq. 20) yields a positive definite system of equations which is solved using Gaussian elimination. The **A** matrix is independent of the boundary conditions so that it is only calculated once. The system of equations is solved once for each poloidal harmonic (see Eq. 9) and only once for the antenna contribution (see Eq. 10).

2.4 Test cases

In this section we will describe some test cases for the new module in CASTOR which calculates the vacuum response due to an external antenna. In cylindrical geometry the vacuum equations can be solved analytically. The solution is given by

$$
\begin{aligned}
\hat{b}_\phi(r < r_a, \theta) &= in\left(\frac{f_i(r)}{f_i'(r_p)}b_r + \left(f_d(r) - \frac{f_d'(r_p)}{f_i'(r_p)}f_i(r)\right)j_\theta\right)e^{im\theta} \\
\hat{b}_\phi(r > r_a, \theta) &= in\left(\frac{f_i(r)}{f_i'(r_p)}b_r - \frac{f_d'(r_p)}{f_i'(r_p)}f_i(r)j_\theta\right)e^{im\theta} \\
f_i(r) &= I_m(r) - \frac{I_m'(r_w)}{K_m'(r_w)}K_m(r) \\
f_d(r) &= \frac{K_m'(r_a)I_m(r) - I_m'(r_a)K_m(r)}{K_m'(r_a)I_m(r_a) - I_m'(r_a)K_m(r_a)}.
\end{aligned}
\tag{21}
$$

The functions I_m and K_m are modified Bessel functions, r_p, r_a, and r_w are the plasma, antenna, and ideally conducting wall radii. This solution clearly shows the two independent

solutions which contribute to the total vacuum solution. One part of the solution is linear in the perturbed magnetic field on the plasma boundary and independent of the antenna. The other part is linear in the antenna current and independent of the radial magnetic field on the plasma boundary, b_r.

In Fig. 5a the analytic solution of Eq. (21) is compared to the numerical solution as obtained with the CASTOR code for both independent solutions. Excellent agreement is found; the convergence rate of the relative error as a function of the number of gridpoints N_g scales as $\sim N_g^{4.5}$ for both solutions.
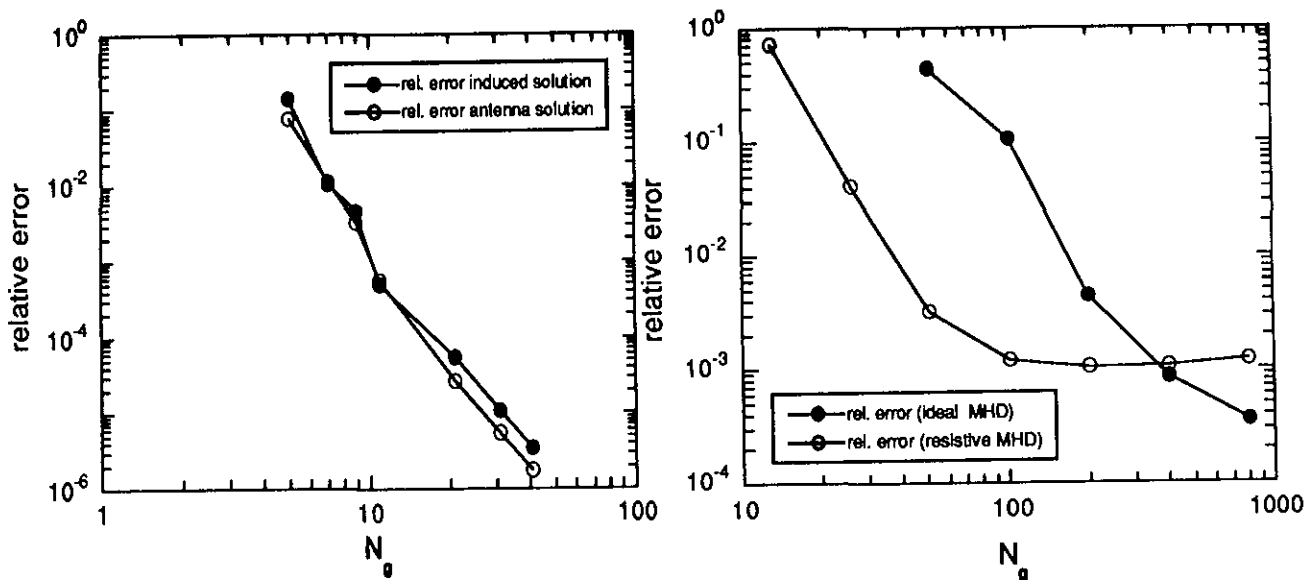
Fig. 5a *The relative error in the numerical solution compared with the analytic solution in a cylinder as a function of the number of gridpoints. ($n/m = -1/2, r_p = 0.05, r_a = 0.06, r_w = 0.075$)* **Fig. 5b** *The relative error in the power absorbed by the plasma compared numerical solution of the LEDA code for ideal and resistive MHD. ($\rho = 1 - 0.8r^2, q_0 = 1$, aspect ratio $= 20$, ideal case : $J(r) = 0.1, \omega = 0.25 + 0.001i$, resistive case : $j(r) = 0.1(1 - r^2), \omega = 0.18, \eta = 5 \times 10^{-8}$)*

An important diagnostic of the response problem in the CASTOR code is the power absorbed by the plasma

$$P = -\tfrac{1}{2} \iiint_{\text{vac}} j \cdot E^* dV \qquad (22)$$

13

where j is the current and E the electric field inside the vacuum. The integral is over the vacuum volume. A more practical expression in terms of the magnetic fields at the antenna surface is given by :

$$P = 2\pi^2 \sum_m \lambda [\![\Phi_m]\!] (Jb^1)_m^*$$

(23)

where J is the jacobian of the vacuum coordinate system and b^1 is the radial contravariant component of the magnetic field at the antenna surface and $[\![\Phi_m]\!]$ is the jump in the magnetic potential at the antenna. Fig. 5b compares the relative error in the power as calculated by the cylindrical code LEDA [5] with the values obtained with the CASTOR code.
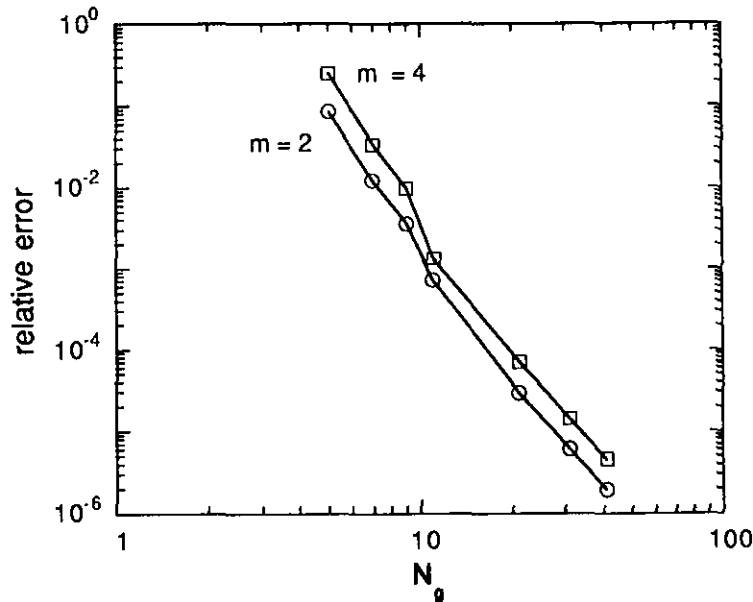
Fig. 5c   *The relative error in the numerical solution compared with the analytic solution in a straight elliptical plasma as a function of the number of gridpoints. ($n = 0, \mu_p = 0.8047, \mu_a = 0.93, \mu_w = 1.1$, driving antenna current $m = +2$ and $m = -2$, m ranges from -15 to +15.)*

In the cylindrical test case, the poloidal harmonics, m, of the solution are independent. To test the coupling of the different harmonics, we can use the analytic solution of the vacuum equations for the case of a straight elliptical plasma with a constant current. The CASTOR angular coordinate at the plasma boundary is in that case identical to the

14

angular coordinate of the separable elliptical coordinates. Taking both the shape of antenna surface and the wall to be a coordinate surface, the analytic solution is similar to the cylindrical solution except that the Bessel functions, K_m and I_m, are replaced by $e^{m\mu}$ and $e^{-m\mu}$, where μ is the radial coordinate of the elliptical coordinate system. Note that, although the different harmonics are independent in the analytic solution, this is not the case for the CASTOR coordinate system. The results of the comparison of the analytic and the numerical solutions are shown in Fig. 5c. The error decreases with increasing number of grid points as $\sim N_g^5$.

As a final test case we have made a comparison of the results of the driven version of the CASTOR code with those given by the LION code [6], an existing code for calculating the plasma response to an external antenna. These results were kindly made available to us by L. Villard. Both codes make use of a stationary MHD equilibrium which is found numerically by using another code. (CASTOR uses the equilibrium as given by HELENA, LION uses as an input the solution of the equilibrium as found by CHEASE). There are two major differences between CASTOR and LION. The first one is that the codes use a different model for the plasma perturbations; CASTOR uses the linearized resistive MHD equations, and LION uses a cold, current carrying plasma dielectric tensor, neglecting electron inertia. When the frequencies used are much smaller than the ion-cyclotron frequency this model should be the same as the ideal MHD model in which the ratio of specific heats is set to zero. Acoustic waves are not described by this model. The second difference is of numerical nature: while CASTOR uses finite elements for the radial dependence and a Fourier-expansion in the poloidal angle, LION makes use of a two dimensional grid on which 2-D finite-elements are used to represent both the radial and the poloidal dependence of the perturbations.

The equilibrium used in this test case consists of a circular Soloviev equilibrium with a constant density profile. The inverse aspect ratio is taken to be 0.3 and the safety-factor at the magnetic axis is set to 1.1. In order to be able to calculate the frequencies at which resonances are positioned the following physical quantities are chosen: $B_0 = 3\text{T}, R_0 = 3.1\text{m}, n_0(D) = 3.5 \times 10^{19}\text{m}^{-3}$.

Using this equilibrium a scan is made of the plasma response to frequencies in the lower part of the Alfven continuum for toroidal modenumber $n = -1, -2, -3$ and a helical current in the antenna with poloidal modenumber $m = |n| + 1$. Instead of using a resistive plasma in which, in the stationary state, the absorbed power equals the ohmic dissipation, so-called artificial damping is introduced by using a complex driving frequency with a small imaginary part. In the limit of small artificial damping the damping rate is identical to the

15

damping rate found in the limit of small resistivity. The advantage of using an artificial damping is that the position of the resonances is independent of the value of the artificial damping. This is not the case for a resistive plasma.

We investigate the resonances to find their position and width when the artificial damping goes to zero. The damping is found from the halfwidth at halfheight (HWHH) of the resonance. The results are shown in Table 1.

n	LION frequency [kHz]	LION HWHH/freq	CASTOR frequency [kHz]	CASTOR HWHH/freq
-1	?	strongly damped	139.3	0.
-1	277.7	0.	291	< 1E-3
-1	394.0	0.	393	< 1E-3
-1	509.0	< 2E-3	536.9	< 1E-3
-2	~ 97	~ 0.2	~ 50	~ 0.5
-2	311.3	1.4E-2	319	8.3E-3
-2	385.8	< 2E-3	390	< 2E-3
-3	80.5	4.6E-2	83.1	0.6E-2
-3	291.9	< 4E-3	~ 300	?

Tabel 1 *Comparison of the frequencies of the global Alfvén modes of the circular Soloviev Equilibrium as calculated with the LION code and the CASTOR code*

The following remarks can be made: For $n = -1$ we find that all the global modes are situated in the gaps in the Alfven continuum. The positions of the gaps as found by CSCAS (a code which calculates the local Alfven frequencies belonging to a given equilibrium as a function of the minor radius [7]) are given in Table 2.

$n = -1$	$n = -2$	$n = -3$
85 - 290 kHz	115 - 255 kHz	135 - 230 kHz
330 - 400 kHz	375 - 395 kHz	~ 375 kHz (almost closed)
515 - 590 kHz		

Tabel 2 *The continua of the Soloviev equilibrium as calculated with the CSCAS code*

The LION code finds for $n = -1$ at low frequencies a mode which lies below the first gap and is therefore strongly damped. We do not find such a mode but instead find one

which is undamped and well within the gap. For $n = -2$ the two modes with the lowest frequencies are within the continua and damped. The mode with the highest frequency lies in a gap and is undamped. Finally for $n = -3$ two modes are found, both in the continuum part of the spectrum. The one at 300 kHz coincides with the frequency at which a part of the $m = 4$ continuum sets in and can hardly be distinguished from the background which corresponds to the power absorbed by continuum modes. In this case the LION code finds an (almost) undamped mode. We conclude that both codes (LION and CASTOR) find the same resonances, but that there are some discrepancies in the exact position and damping of the modes found. These discrepancies can probably be explained by the difference in the codes and the sensitivity of the damping on the position relative to the continuum. So the comparison between the codes is satisfactory, considering the difference in the models.

3 APPLICATION TO THE JET SADDLE COILS

During the 1991/92 shutdown of JET, saddle coils have been installed in the JET vessel for disruption control. For this the coils are driven by a high power (~ 1 MW) amplifier in a typical frequency range of 0 - 10 kHz. The same coils can be used for the excitation of global Alfvén waves in the plasma. The typical frequency range is 30 to 500 kHz at a typical power level of several kiloWatts.

In this chapter, we apply the extended CASTOR code to model the excitation of modes in JET plasmas with the saddle coils. A complete spectrum of the plasma response as 'measured' by the absorbed power is discussed for a JET discharge and physical values of quantities (impedance, mode amplitude) relevant to the experiment are calculated.

3.1 Modelling of the saddle coil currents

The JET saddle coils consist of eight coils, four in the toroidal direction both at the top and bottom of the vessel. By switching the relative phases, toroidal mode numbers of $n = -1$ and $n = -2$ can be produced as the main harmonics. Other mode numbers will also be present as side bands. The poloidal mode number is by construction dominantly $m = 2$ with $m = 4$ and $m = 0$ as the most important side bands.

In CASTOR, due to the axisymmetric equilibrium, the saddle coils can be modelled as a sum of independent helical antennas with different toroidal mode numbers. Fig. 6a shows the current distribution of the saddle coils in the (θ, ϕ) plane through the saddle coils in the $n = 1$ phasing. Here, the total current distribution is represented with 8 Fourier harmonics in the toroidal direction and 31 Fourier harmonics in the poloidal angle. The localized nature of the saddle coils currents is well represented by this Fourier series.

17
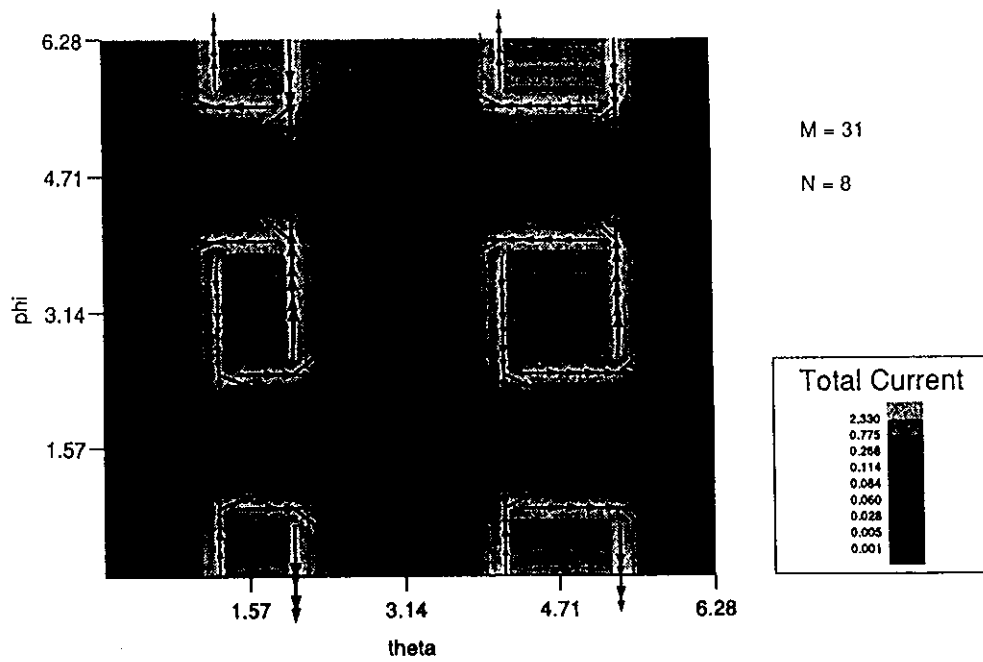
Fig. 6a *The current distribution in the JET saddle coils in the n = 1 configuration,*
represented by 9 toroidal and 31 poloidal Fourier harmonics.
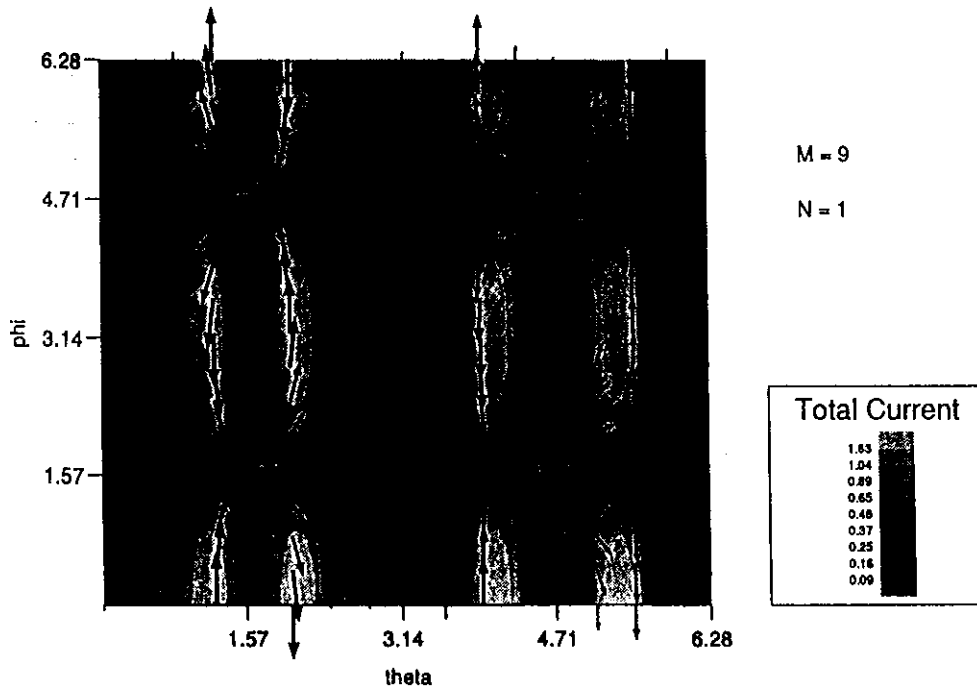
Fig. 6b *The n = 1 component of the saddle coil current distribution in n = 1*
phasing, using 9 poloidal Fourier harmonics.

18

In Fig. 6b the current distribution is shown from the $n = 1$ harmonic using 9 poloidal harmonics. This corresponds to a typical number of Fourier modes which is feasible in the CASTOR calculations. The localized nature of the saddle coil currents in the poloidal angle is very well preserved. The return currents in the poloidal direction become less localized for each toroidal harmonic separately.

3.2 Excited spectrum with JET saddle coils

A major advantage of the antenna extension of the CASTOR is that it enables the study of global modes which are well inside a continuum. Specifically, with a finite pressure, the lower frequency global modes will lie inside the slow continuum. For spectral (eigenvalue) codes it is very difficult to find the global modes inside the multitude of singular continuum modes. For this reason, the slow continuum is often suppressed by either studying low-β plasmas or incompressible plasmas. With the driven (antenna) version of the CASTOR code, these global modes are easily found as sharp maxima in the power that is absorbed by the plasma. The damping of the modes is obtained from the half width at half height of the maxima. Thus, the extended CASTOR code is ideally suited to study the effect of a finite pressure on the position and the damping of the global modes.

To study the effect of high β the high performance discharge 26087 is analysed keeping the effects of a finite pressure. This discharge has a toroidal beta of 2.5%, at about 80% of the Troyon limit.

The continuum frequencies of this discharge, obtained with the CSCAS code [7], are plotted in Fig. 7 as a function of the minor radius. At this high value of the pressure, the slow continua, which are linear in the local pressure and the ratio of the specific heats γ , overlap the Alfvén continuum and the lowest Alfvén gap. The interaction of the slow and the Alfvén continua breaks up the lowest Alfvén continuum and the separation between the slow and Alfvén branches disappears. Due to the interaction of the slow and Alfvén branches a new gap opens up around $\omega/\omega_a = 0.20$.

The frequency of the slow continua increases with the poloidal modenumber m. So in principle, the ellipticity induced gap is also covered by the slow continua. In this case, however, this happens only for mode numbers m larger than four (not drawn in the Fig. 7). The interaction of the slow modes with the lower m Alfvén modes is very weak in this case.

19
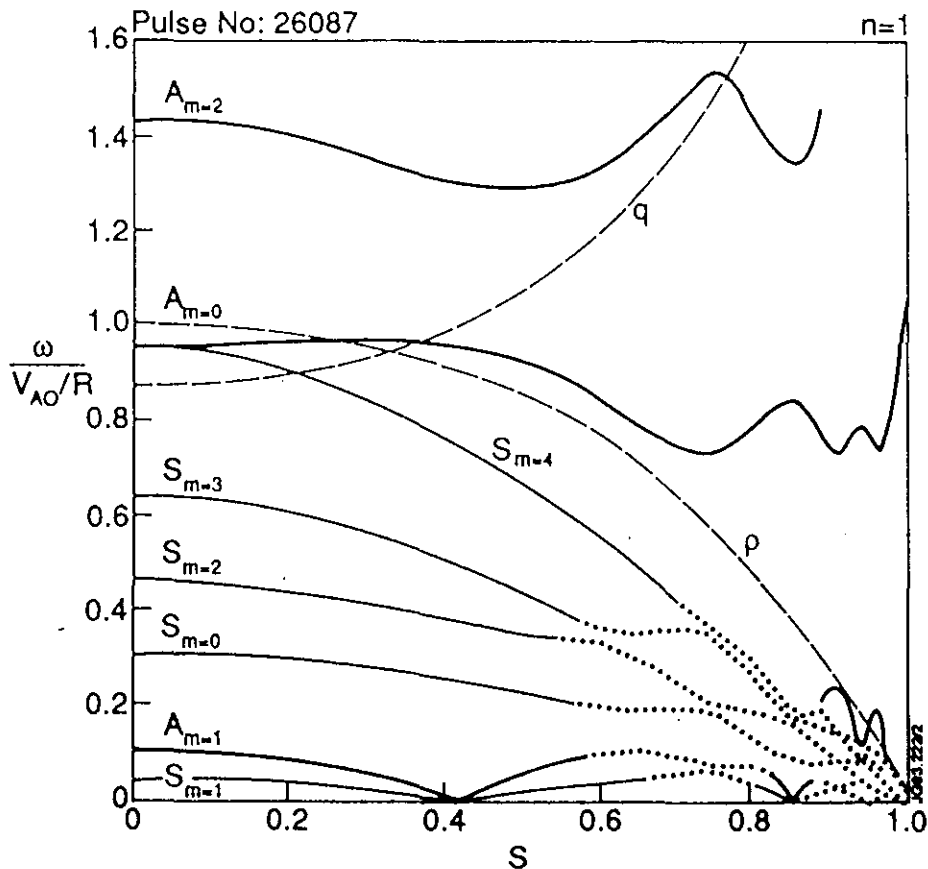
Fig. 7 The slow (thin lines) and Alfvén (fat lines) continua as a function of the radial coordinate $s = \sqrt{\psi}$ of JET discharge 26087. The q-profile and the density profile are also drawn. The index to the slow (S) and Alfvén (A) continua indicates the main poloidal harmonic. The dotted lines represent the continua with a strong interaction between Alfvén and slow branches.

3.2.1 The TAE and EAE modes; the influence of a finite pressure

This discharge is now, numerically, excited with the saddle coils as the external antenna in the $n = 1$ configuration. The complete spectrum of the plasma response due to the predominantly $m/n = 2/1$ magnetic field perturbation induced by the antenna is shown in Fig. 8.

The toroidal Alfvén eigenmodes (TAE) have the frequencies $\omega = 0.35, 0.41$ and 0.72. The TAE mode at $\omega = 0.35$ lies on the edge of the lower 'Alfvén' continuum and is heavily damped. In the case of an incompressible plasma, i.e. no interaction of Alfvén and slow modes, the TAE gap is completely open and the TAE mode at $\omega = 0.40$ experiences no continuum damping. In a compressible plasma, however, the mode interacts with the slow/Alfvén continuum and does have a singularity in the dominant harmonic $m = 2$. The eigenfunction of this TAE mode is shown in Fig. 9a. The continuum damping due to these

20

(slow) singularities turns out to be small ($< 2 \times 10^{-3}$). Fig. 10 shows the resonance peaks for three values of the resistivity. The damping due to the slow continua is small due to the parallel polarization of slow continuum modes for which continuum damping (i.e. phase mixing) is much less efficient. From this, it is clear that almost undamped TAE modes can still exist in relevant discharges at a pressure close to the Troyon limit.
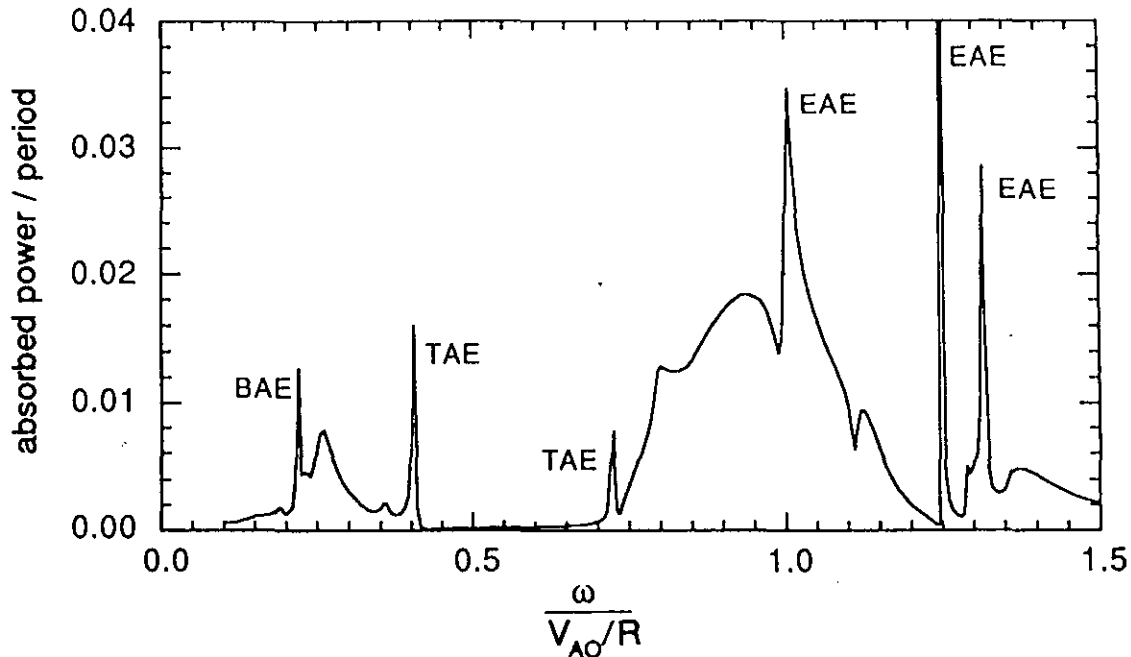
Fig. 8 *The power absorbed by the plasma as a function of the antenna frequency. The Alfvén frequency is 332 kHz. The plasma resistivity η is 10^{-7}, the toroidal mode number $n = 1$.*

Above $\omega = 0.75$ the second Alfvén continuum sets in. This causes the increased background in the absorbed power up to $\omega = 0.97$. The large peaks between $\omega = 1.0$ and 1.35 are due to ellipticity induced eigenmodes (EAE). The eigenfunction of the undamped EAE at $\omega = 1.25$ is shown in Fig. 9b. Above $\omega = 1.35$ the third Alfvén continuum exists.

3.2.2 A pressure driven mode; the BAE mode

In the lowest, pressure induced, gap, we find a sharp resonance at $\omega = 0.22$. This resonance is due to a global mode inside the gap of the $m = 0$ and $m = 2$ slow and $m = 1$ Alfvén gap, i.e., the global mode has a large $m = 1$ and $m = 2$ component (see Fig. 9c). This resonance disappears if the plasma is incompressible. A similar, pressure

21
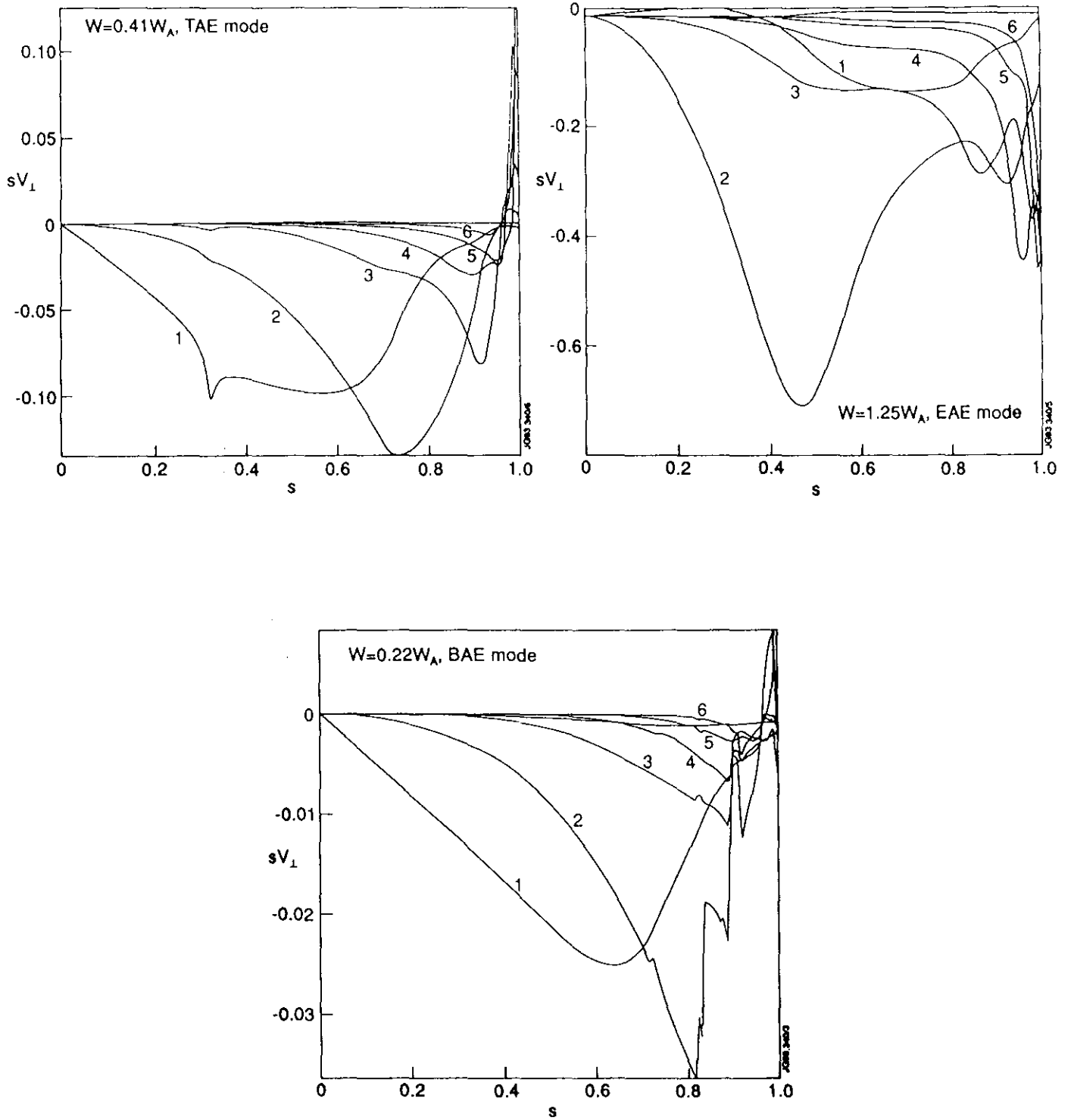
Fig. 9 a) *The eigenfunctions of the normal velocity as a function of the minor radius coordinate $s = \sqrt{\psi}$ for a) the TAE mode, b) the EAE mode, and c) the BAE mode. The resistivity is 10^{-7}.*

22

driven, mode has been found in [2], where it is called a BAE mode (for beta induced Alfvén eigenmode). The mode at $\omega = 0.22$ is, however, not a clear Alfvén mode. The influence of the slow continuum is clearly seen in the polarizat'on of the mode. The ratio of the parallel to perpendicular component of the displacement is a factor of 10 larger than that of the pure Alfvén mode at $\omega = 0.40$. The continuum damping of this mode is small. However, at these relatively low frequencies, the contribution of ion Landau damping is expected to become dominant. Therefore, this global mode is not expected to be relevant with respect to α-particle instabilities.
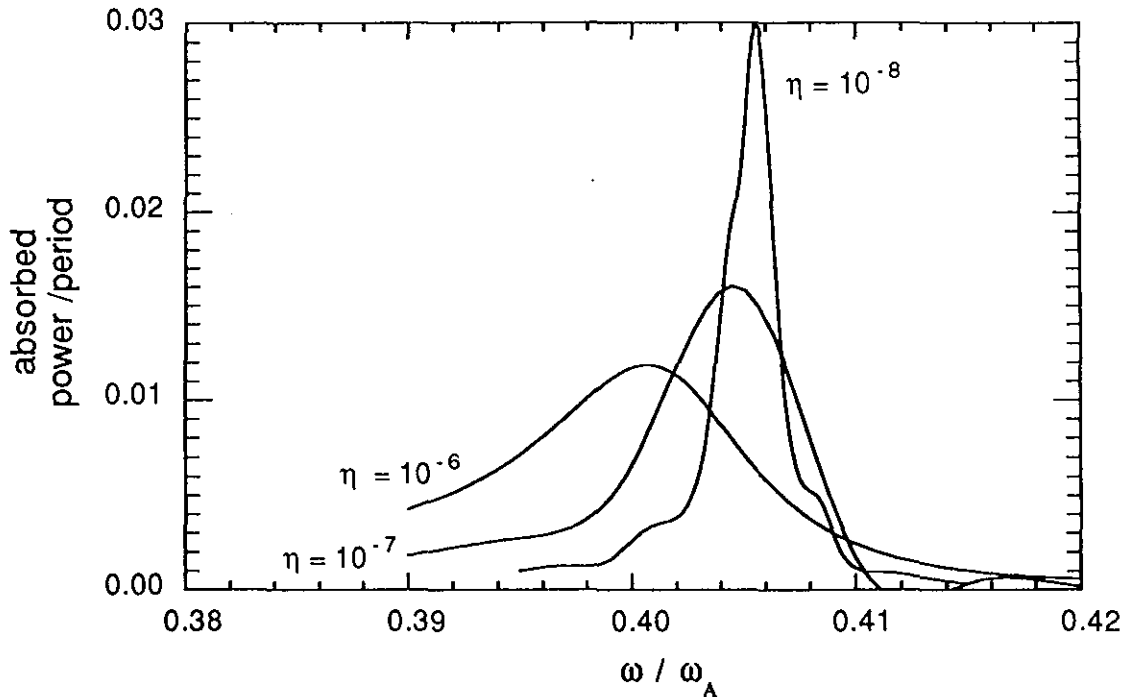
Fig. 10   *The power absorbed by the plasma as a function of the antenna frequency for three values of the resistivity. The other parameters are the same as in Fig. 8*

4   CONCLUSION

In order to model the excitation of Alfvén waves in a plasma the toroidal resistive MHD code CASTOR has been extended to include an external antenna. The plasma response induced by the JET saddle coils as the external antenna can now be accurately calculated for general JET discharges, providing a excellent tool for the study of what has been termed 'MHD spectroscopy' [8].

The first results show that global Alfvén modes can be excited by the JET saddle

coils. The plasma response as measured by the antenna impedance (the power absorbed by the plasma) shows resonances at the global mode frequencies. The ellipticity induced eigenmodes show a larger response than the toroidicity induced eigenmodes.

The newly developed 'driven' version of the CASTOR code is not only useful to study the excitation of modes by an external antenna, it is also a very powerful code to study the TAE and EAE modes and their damping. With a spectral code it is very difficult to locate global modes which lie inside a continuum. With a antenna (response) code, however, these global modes are easily resolved.

The effect of a finite pressure in a compressible plasma was investigated. The dominant effect is the overlap of the Alfvén gaps and continua by the slow mode continua. The additional singularities in the global modes caused by the slow continua does however not significantly increase the continuum damping rate. The second effect of the pressure is to create a new gap below the lowest (toroidicity induced) gap. This gap is due to the interaction of the slow and Alfvén continua. Inside this gap a new type of global mode was found. This mode is pressure driven and is not there in an incompressible plasma.

references

[1] K.L. Wong et al., Phys. Rev. Lett. **66**, 1874 (1991).

[2] A.D. Turnbull et al., General Atomics report, GA-A21138 (1992).

[3] W. Kerner, S. Poedts, J.P. Goedbloed, G.T.A. Huysmans, B. Keegan, and E. Schwartz, Contr. Fusion and Plasma Physics, (1991), 18th Eur. Conf. Berlin, part IV, p.89.

[4] G.T.A. Huysmans, J.P. Goedbloed and W. Kerner, Phys. Fluids B (1993), **5**, 1545.

[5] S. Poedts, W. Kerner, and M. Goossens, J. Plasma Physics (1989), **42**, 27.

[6] L. Villard, K. Appert, R. Gruber, and J. Vaclavik, Comp. Physics Reports 4 (1986) 95-135.

[7] S. Poedts and E. Schwartz, J. Comp. Phys. (1993), Vol.105, No.1, 165.

[8] J.P. Goedbloed, Trends in Physics, Vol. III, (EPS, Praag, 1991), p.827.